ACS OMEGA

http://pubs.acs.org/journal/acsodf

Article

Hierarchical Porous Carbon-PtPd Catalysts and Their Activity toward Oxygen Reduction Reaction

Ofelia Marilu Arias-Pinedo, Andy A. Cardenas Riojas, Elena Pastor, Elvis O. López, Geronimo Perez, Braulio S. Archanjo, Miguel Ponce-Vargas, Gabriel Ángel Planes, and Angélica María Baena-Moncada*

Cite This: *ACS Omega* 2022, 7, 20860−20871

Read Online

ACCESS | Metrics & More | Article Recommendations | Supporting Information

ABSTRACT: PtPd bimetallic catalysts supported on hierarchical porous carbon (HPC) with different porous sizes were developed for the oxygen reduction reaction (ORR) toward fuel cell applications. The HPC pore size was controlled by using SiO_2 nanoparticles as a template with different sizes, 287, 371, and 425 nm, to obtain three HPC materials denoted as HPC-1, HPC-2, and HPC-3, respectively. PtPd/HPC catalysts were characterized by scanning electron microscopy, X-ray photoelectron spectroscopy, X-ray diffraction, and high-resolution transmission electron microscopy. The electrochemical performance was examined by cyclic voltammetry and linear sweep voltammetry. PtPd/HPC-2 turned out to be the most optimal catalyst with an electroactive surface area (ESA) of 40.2 $m^2\ g^{-1}$ and a current density for ORR of −1285 A g^{-1} at 2 mV s^{-1} and 1600 rpm. In addition, we conducted a density functional theory computational study to examine the interactions between a PtPd cluster and a graphitic domain of HPC, as well as the interaction between the catalyst and the oxygen molecule. These results reveal the strong influence of the porous size (in HPC) and ESA values (in PtPd nanoparticles) in the mass transport process which rules the electrochemical performance.

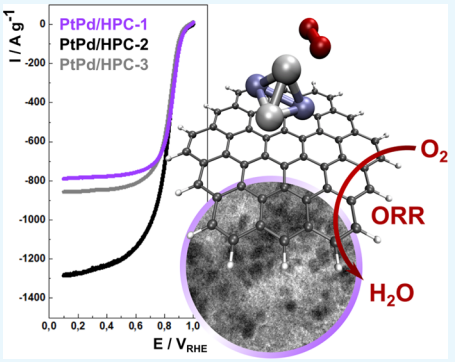

1. INTRODUCTION

The consumption of fossil fuels, such as reserves of oil, gas, and even easily extracted carbon[1−3] has significantly raised greenhouse gas emissions causing a global average temperature increase of around 1 °C.[4] Therefore, it is necessary to obtain efficient alternative sources of energy, such as fuel cells (FC), that use electrochemical processes for the conversion of chemical energy into electrical energy from a fuel oxidation reaction.[5−7] In addition, proton exchange membrane FC, direct methanol FC (DMFC), and alkaline FC have attracted increasing attention over the past decades due to their high power density and high efficiency in energy conversion.[8−10] However, the biggest challenge is still improving their cost and durability. A key factor in DMFC design is the choice of the catalysts employed as electrodes.[11] Due to the catalytic properties of Pt-based nanomaterials, they are the most widely used electrocatalysts to accelerate the oxidation of the fuel at the anode and the reduction of oxygen at the cathode.[12] The oxygen reduction reaction (ORR) is widely considered the most relevant reaction in FC, which must fulfill three key requirements: to be active, selective, and long lasting.[11,13] However, the slow oxygen reduction kinetics at the cathode is a concern that still restricts the widespread commercialization of FC.[10]

To decrease Pt load and prevent catalyst agglomeration, the noble metal is supported on porous carbon-based materials, where the support avoids the reduction of the active surface area, which is related to the catalytic performance and facilitates mass transport.[12,14] Therefore, to optimize the catalytic activity, reduce the cost and increase the durability of Pt-based catalysts, new bi, tri, or multimetallic nano-catalysts are used.[10,15,16] There is a vast amount of literature on Pd/Pt alloys due to their excellent catalytic activity, stability, and durability to be used in ORR compared to commercial Pt/C, and they can be easily synthesized in different structures and compositions.[12,17] Pd/Pt nanosheets have specific mass catalytic activity 2.2 times higher than commercial Pt/C with a lower loss of mass activity (18.9 vs 50%) considering 10,000 cycles with the catalytic activity of 0.74 mA cm^{-2} at 0.9 V.[18] Pd/Pt nanoflowers have a large surface area and lower density which provides more reaction sites reaching a specific activity of 0.70 mA cm^{-2} after 500 cycles with a loss of 1.6%, compared to 35.2% of the Pt/C in current density,[19] and those that are supported on graphene oxide exhibit up to 70% catalytic activity (even up to 5 °C) compared to 57% of Pt/C.[20] Also, Pd/Pt nanocrystals supported on ionic polymer functionalized graphene exhibit improved ORR activity (specific activity: 1.89

Received: March 10, 2022
Accepted: May 11, 2022
Published: June 7, 2022

mA cm^{-2} at 0.9 V_{RHE}) and greater durability with respect to commercial Pt/C (specific activity: 0.23 mA cm^{-2} at 0.9 V_{RHE}).[21] Remarkably, Pd/Pt nanospheres supported on reduced graphene oxide (rGO-PtPd) exhibit a higher surface than Pt/C black (1.68:1), resulting in a greater specific activity of 0.54 versus 0.32 mA cm^{-2}.[22]

Another way to improve ORR is to support the catalysts in porous carbon, specifically, hierarchical porous carbons (HPCs). These promising materials present pores with sizes between 2 and 500 nm, with adjustable void spaces to avoid agglomeration and allow easy control of the metal catalyst load. The void spaces also promote the diffusion and migration of reactants and products inside the carbon matrix during the ORR reactions.[23,24] For example, HPC materials doped with different elements such as Fe, N, and P exhibit an ORR behavior similar to commercial catalyst Pt/C, reaching current densities in the same order of magnitude, without using a noble metal. The catalytic efficiency of these materials is due to the combination of micro, meso, and macropores structures that promotes the oxygen transfer and diffusion to the active sites.[25−28] In the case of catalysts supported on carbon materials and HPC, results for Co and the bimetallic PtCo and PtPd are remarkable. These materials exhibit similar values of current densities relative to the commercial Pt/C, but with an increase in catalyst stability.[29−33]

In this work, PtPd nanoparticles supported on HPCs with different porous sizes are evaluated as ORR catalysts, given the still unclear relationships among pore dimensions, mass transport, and catalytics performance in FC cathodes. The catalyst characterization was conducted by surface and bulk techniques such as scanning electron microscopy−energy-dispersive X-ray spectroscopy (SEM−EDX), high-resolution transmission electron microscopy−EDX (HRTEM−EDX), X-ray photoelectron spectroscopy (XPS), and X-ray diffraction (XRD), which are important tools in the characterization of PtPd composites. The influence of the surface electroactive area of PtPd nanoparticles and the HPC porous sizes in the ORR efficiency was evaluated by linear sweep voltammetry (LSV). Finally, a computational study in the framework of density functional theory (DFT) provides insights into the interaction between the bimetallic catalyst and a graphitic domain of HPC, as well as the interaction between the catalyst and the oxygen molecule.

2. METHODOLOGY

2.1. Synthesis of Hierarchical Porous Carbon. SiO_2 nanoparticles (SiO_2-NPs) of different sizes (300, 400, and 500 nm) were used as templates for the synthesis of the HPCs. The synthesis of SiO_2-NPs was carried out by the Stôber method,[34] where a tetraethyl orthosilicate (TEOS) solution 0.4 mol L^{-1} in ethanolic medium (solution 1) was mixed with an ethanolic solution of ammonium hydroxide 0.4 mol L^{-1} and water 34 mol L^{-1} (solution 2). Both solutions were gently mixed at room temperature for 6 h.[35] The obtained SiO_2-NPs were washed with ethanol at pH ∼ 7. This process was repeated with ammonium hydroxide 1.2 and 3.04 mol L^{-1} in order to obtain SiO_2-NPs of different sizes.

The resulting SiO_2-NPs was thermally treated to form an interconnected opal at 1000 °C in the presence of oxygen. Then, SiO_2 opals were impregnated with the resorcinol/formaldehyde resin. This resin is made up of a mixture of 1.0 g of resorcinol, 1.6 mL of formaldehyde, and 0.4 mL of 0.1 mol L^{-1} sodium carbonate as a catalyst. Then, a post-treatment was carried out at 100 °C. The samples were then placed in a furnace and carbonized at 850 °C under an inert atmosphere for 24 h. Finally, the SiO_2-NP template was removed through treatment with 10% hydrofluoric acid in an ethanol/water medium (1:1).[36]

2.2. Pt/Pd Catalysts Supported on Hierarchical Porous Carbon. For the synthesis of the PtPd/HPC catalysts, 100 mg of HPC with sizes of 300, 400, and 500 nm were weighted, and a mixture containing 348 μL of H_2PtCl_6 and 77.33 mg of $PdCl_2$ in 50 mL of water was added. This mixture was left stirring for approximately 12 h. Then, the pH was adjusted to 5 by adding NaOH (final volume ∼ 70 mL) and stirring was continued for 6 h. The reduction was carried out using $NaBH_4$ (50 mg/50 mL of H_2O) as the reducing agent, 1 mL was added every 3 min, and stirring was continued for about 24 h. Finally, the obtained catalyst was filtered, washed with distilled water, and dried.

2.3. Structural, Chemical, and Morphological Characterizations. The size of the synthesized silicon oxide nanoparticles was measured by the dynamic light scattering (DLS) technique with Particle Sizing Systems, Inc. The thermogravimetric Analysis−differential scanning calorimetry (TGA−DSC) study of carbon material was performed by PerkinElmer equipment, in a temperature range of 25−1000 °C in the presence of O_2. Raman spectroscopy measurement was obtained using HORIBA Scientific equipment, with a laser length of 532 nm and a laser power of 10%.

Catalyst morphologies were obtained by SEM using a Carl Zeiss EVO 10-MA with an EDX micro-analyzer, Oxford-INCA.

Diffraction patterns were obtained by a PANalytical X'Pert diffractometer using a polychromatic X-ray of Cu $K\alpha_{1,2}$ and in Bragg−Brentano configuration, 2θ values ranging from 20 to 80° at a step size of 0.02°. The lattice parameter a and crystallite size were calculated from Rietveld refinements using FullProf software. The Pt/Pd crystallographic parameters (space group, atomic positions, and unit cell parameters) reported in the literature[37] were used to initiate the refinement of these three materials. A pseudo-Voigt profile function was used to model the Bragg reflection peak shapes. The background was manually selected using the WinPLOTR program. The maximum theoretical occupancies for Pt and Pd were fixed according to the appropriate Wyckoff positions sharing an occupancy of 1.

Analytical measurements of the functional ionic groups in the samples were made from Fourier transform infrared spectroscopy (FTIR), using a Shimadzu model IR-Prestige 21 equipment. Measurements were made by the transmission mode using the KBr powder. The measurement conditions were as follows: wavelength range between 400 and 4000 cm^{-1}, resolution of 4 cm^{-1}, and scan of 150 times per sample.

XPS measurements for metal oxidation states of PtPd/HPC were carried out using a Thermo Scientific spectrometer with Al $K\alpha_{1,2}$ radiation. The high-energy resolution binding energy obtained at C 1s, O 1s, Pt 4f, and Pd 3d lines was 0.1 eV. Due to good material conductivity, the use of a flood gun was not necessary. In this way, the C 1s line at a binding energy of 284.7 ± 0.1 eV was used for energy calibration. For fitting the peaks of palladium and platinum, the difference between the $3d_{5/2}$ and $3d_{3/2}$ levels (5.26 eV) as well as that between $4f_{7/2}$ and $4f_{5/2}$ levels (3.33 eV) were considered.

Transmission electron microscopy (TEM) studies were conducted using a Fei Tecnai Spirit transmission electron

https://doi.org/10.1021/acsomega.2c01457
ACS Omega 2022, 7, 20860−20871

microscope operating at 120 kV and a probe-corrected Fei Titan equipped with an energy-dispersive X-ray spectroscope operating at 300 kV on TEM and scanning TEM (STEM) modes. The samples were diluted in ethanol and sonicated for a while, and finally, a single drop was placed in a conventional TEM copper grid having a thin holey carbon film.

2.4. Electrochemical Characterization. The PtPd/HPC catalysts were prepared from an aqueous suspension containing 2 mg mL^{-1} of the catalyst in 15 μL of Nafion (5 wt %, Aldrich) and 500 μL of distilled water. An aliquot (10 μL) of the suspension was deposited on a glassy carbon disk (φ = 3 mm) in order to cover its entire surface and dried at room temperature under an Ar atmosphere.

Electrochemical measurements were carried out using an Autolab PGSTAT30 potentiostat−galvanostat, in a conventional three-electrode cell: a glassy carbon plate with a high surface area was used as an auxiliary electrode; a 3 mm diameter glassy carbon disk as the working electrode; a normal hydrogen electrode RHE as the reference electrode, and H_2SO_4 0.5 mol L^{-1} is the supporting electrolyte. The electrochemical active areas of the catalysts were measured from the CO stripping by integration of the oxidation peak, assuming a load of 420 μC cm^{-2}. These electroactive areas were then used to calculate the current densities J (mA cm^{-2}). CO was adsorbed at 0.2 V, bubbling this gas in the electrolyte for 15 min. The CO excess was removed from the solution by bubbling Ar gas for 20 min, keeping control of the potential. Finally, it was cycled between 0.05 and 1.0 V at 20 mV s^{-1}, and the current of the oxidation peak was integrated. The electroactive surface area (ESA) values were divided between the amount of catalyst present in the electrode according to EDX analysis in order to express them in m^2 g^{-1} for the sake of comparison.

Polarization curves for the electrochemical oxygen reduction were made by LSV using O_2 gas (air liquid; 99.995%) between 1 and 0.1 V at 2 mV s^{-1} at different rotation speeds (400, 600, 900, 1600, and 2500 rpm). Before each experiment, oxygen was bubbled for 20 minm, with H_2SO_4 0.5 mol L^{-1} as the supporting electrolyte.

2.5. Computational Study. A computational study in the framework of density functional theory (DFT) has been conducted to estimate the magnitude of the interactions between the PtPd nanoparticles and a graphitic domain of the HPC, as well as the interactions between the catalyst and an oxygen molecule. The DFT calculations were carried out using the Gaussian16 software package,[38,39] tightening self-consistent field convergence thresholds (10^{-10} a.u.). The M06-2X functional[40] and the 6-311G(d)/LANL2DZ basis set were employed for geometry optimizations without symmetry constraints, and the subsequent frequency calculations to ensure that the calculated geometry corresponds to energy minima. The bimetallic nanoparticle was modeled by using the most stable structure of a neutral Pt_2Pd_2 cluster, as proposed by Alexandrova et al.,[41] which interacts with a graphitic domain of HPC, represented by a circumcoronene molecule ($C_{54}H_{18}$). For the overall system, two configurations were considered that differ in the cluster atom (Pt or Pd) pointing to the oxygen molecule. The interaction energy is obtained by a fragments calculation, where the energies of selected fragments are subtracted from the overall energy. The solvent effects of water were included according to the polarizable continuum model[42−44] where the solute is placed in a cavity of molecular shape, and the solvent dielectric response is projected on the surface of such a cavity.

3. RESULTS AND DISCUSSION

SiO_2-NPs were used as templates to obtain HPCs with different porous sizes. The synthesis mechanism consists of catalyzed hydrolysis of TEOS. The reaction starts with chemical hydrolysis and follows the condensation reaction, studied by Stôber.[34,35,45,46]

$$Si(OC_2H_5)_4 + 4H_2OOH^- \rightleftarrows Si(OH)_4 + 4C_2H_5OH \quad (1)$$

$$Si(OH)_4OH^- \rightleftarrows SiO_2 \downarrow + H_2O \quad (2)$$

Figure S1 indicates the dispersion of SiO_2-NP by the hydrodynamic diameter size and shows the average values of the SiO_2-NP diameters (287, 371, and 425 nm, approximately). SEM images of the synthetized carbon obtained using SiO_2-NP as the template are given in Figure S2. For the same magnification, it is observed an increment of the pore diameter as the size of the nanoparticle increases, showing an inverse replica of these templates. The hierarchical porous materials were named HPC-1, HPC-2, and HPC-3 according to SiO_2-NP diameters 287, 371, and 425 nm, respectively.

Figure S3 presents the TGA−DSC and Raman spectroscopy analysis of the different HPCs (HPC-1, HPC-2, and HPC-3). The thermal analysis was performed in the presence of oxygen. A mass loss of HPC materials at a temperature below ∼150 °C is observed (Figure S3a,b), this mass loss can be attributed to the H_2O molecules present in the environment and some volatile organic compounds. The DSC analysis reveals an endothermic process due to the decrease in the heat flow. Between ∼150 and 400 °C, the TGA analysis of the HPCs does not show a noticeable mass loss, except for the HPC-3. The DSC displays a small variation in endothermic heat flux at ∼350 °C. In the range of 400−600 °C, the total oxidation of the HPC occurred, and a notorious endothermic process with a large variation in heat flow due to oxidation is observed. At temperatures above 600 °C, with less than ∼5% mass of HPC remaining, an exothermic process is carried out with an increase in heat flux and ashes formation.[47] Figure S3c indicates the Raman measurement of HPC samples using a 532 nm laser. The intense band at 1600 cm^{-1}, represents the G band typical of sp^2 hybridization, and another weaker G′ band at 2695 cm^{-1} corresponds to the second-order of the G vibration. A D band at 1300 cm^{-1} was also observed along with a D′ + D band at 2900 cm^{-1}. The D band represents the sp^3 hybridization present in the HPC. The shifts of D and G bands (Figure S3c) with respect to the diamond and graphite crystalline structures reveal a disordered structure in the HPC samples. In addition, the weak G′ and D′ + D bands confirm the amorphous structure present in the 3D network of HPC samples.[48]

The synthesis of PtPd/HPC was performed using $NaBH_4$ as the reducing agent, with a PtPd load of 20% in relation to the weight of carbon. By EDX analysis (Figure S4) it was determined that the three synthesized catalysts have a 1:1 ratio with respect to Pt/Pd, although the metallic load displays a variable distribution between 17 and 28.5% in relation to the weight of carbon (Table 1), being PtPd/HPC-1 the catalyst with the highest percent of 28.5%. This value is probably due to the remaining SiO_2 in HPC-1 that was dissolved during PtPd impregnation.

https://doi.org/10.1021/acsomega.2c01457
ACS Omega 2022, 7, 20860−20871

Table 1. Pt/Pd Ratio, Pt−Pd to Carbon Mass Ratio (PtPd/C %) by EDX Analysis

catalyst	Pt/Pd ratio	Pt−Pd/C %
PtPd/HPC-1	53:47	28.5
PtPd/HPC-2	52:48	17.0
PtPd/HPC-3	53:47	17.6

The XRD patterns of the three samples and the Rietveld refinement results are observed in Figure 1 (right). The samples exhibit the (111), (200), (220), (311), and (222) planes that correspond to the face-centered cubic structure (FCC) of the *Fm*3*m* space group. The Rietveld refinement of the XRD patterns was achieved by considering the Pt/Pd ratio obtained by EDX (Figure 1). The refinement determined that Pd^0 has a similar occupancy proportion in the Pt^0 unit cell, confirming a PtPd alloy, see Table 2. Besides, the lattice parameters of the samples were next to the unit cell of Pd^0 (a = 3.8902 Å) related to a microstrain caused by compression ($\varepsilon \approx 2.5 \times 10^3$) observed in all analyzed samples. Furthermore, it was possible to calculate the crystallite size of the materials using the Williamson-Hall method, where the results are in the order of 5 nm for all PtPd nanoparticles (PtPd-NP) (Table 2).

The synthesized PtPd/HPC samples were also characterized by XPS. Figure 2 shows the XPS spectrum at high-energy resolutions of the Pd 3d and Pt 4f lines for the 3 samples.[49,50] The level of Pt $4f_{7/2}$ revealed two adjusted peaks at ∼71.4 and ∼72.6 eV representing typical binding energies (BEs) of metallic (Pt^0) and II (Pt^{2+}) oxidation states, respectively.[51,52] The Pd 3d envelope also exhibits two binding energies (BEs) with Pd $3d_{5/2}$ at ∼335.5 and ∼336.6 eV, which represent the oxidation state of Pd^0 and Pd^{2+}, respectively[51] (see Table 3). The atomic concentration relation at the surface for all elements observed by XPS spectra is presented in Table 3. The

Table 2. Microstructure Parameters of the PtPd/HPC Samples[a]

sample	lattice parameter (Å)	occupation	crystallite size (nm)
PtPd/HPC-1	3.904	Pt = 50%	5.4
		Pd = 50%	
PtPd/HPC-2	3.904	Pt = 50%	4.7
		Pd = 50%	
PtPd/HPC-3	3.894	Pt = 50%	5.9
		Pd = 50%	

[a] Pt^0 lattice parameter, a = 3.9232 Å. Pd^0 lattice parameter, a = 3.8902 Å

Pt^0/Pd^0 ratio for the 3 samples shows a variation between 1.7 and 2.5 that can be attributed to the formation of oxides and other carbon species on the surface. The interface between the PtPd crystalline nanodomains and the HPC was also analyzed by XPS. Table 3 illustrates the presence of COOH− and COH− functional groups with high hydroxide contribution.[51,53] The formation of Pt−OH (Pt^{2+} oxidation state) and Pd−O (Pd^{2+} oxidation state)[51,54] suggests the possibility of OH−Pt−Pd−O−COOH chemical complexes at the surface of PtPd metallic or at the interface between PtPd and HPC structures. By FTIR, O═C−OH− or O═C− ions were not observed (Figure S5), which confirms the hypothesis that PtPd nanoparticles are linked with HPC through OH groups and oxides.

At the nanoscale, the three PtPd/HPC catalysts exhibit similar results with similar PtPd-NP size distribution and moderate aggregation in all samples. Figure 3a shows the TEM image of PtPd-NP on the HPC-2 sample. HRTEM (Figure 3b) images confirm the high crystallinity degree of PtPd-NP with sizes below 10 nm and an average size close to 4 nm, as given in the inset of Figure 3a.

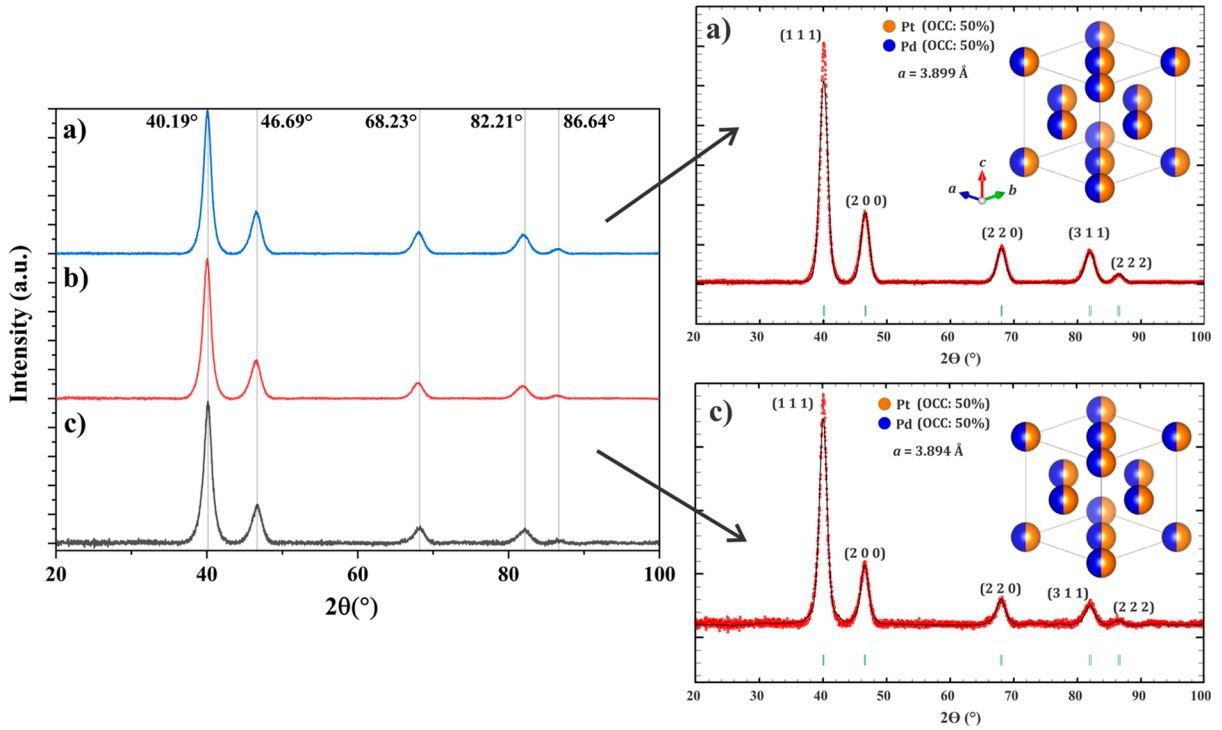

Figure 1. (Left) XRD patterns of (a) PtPd/HPC-1, (b) PtPd/HPC-2, and (c) PtPd/HPC-3 catalysts. (Right) Rietveld refinement using FullProf software of PtPd/HPC-1 and PtPd/HPC-3 samples.

https://doi.org/10.1021/acsomega.2c01457
ACS Omega 2022, 7, 20860−20871

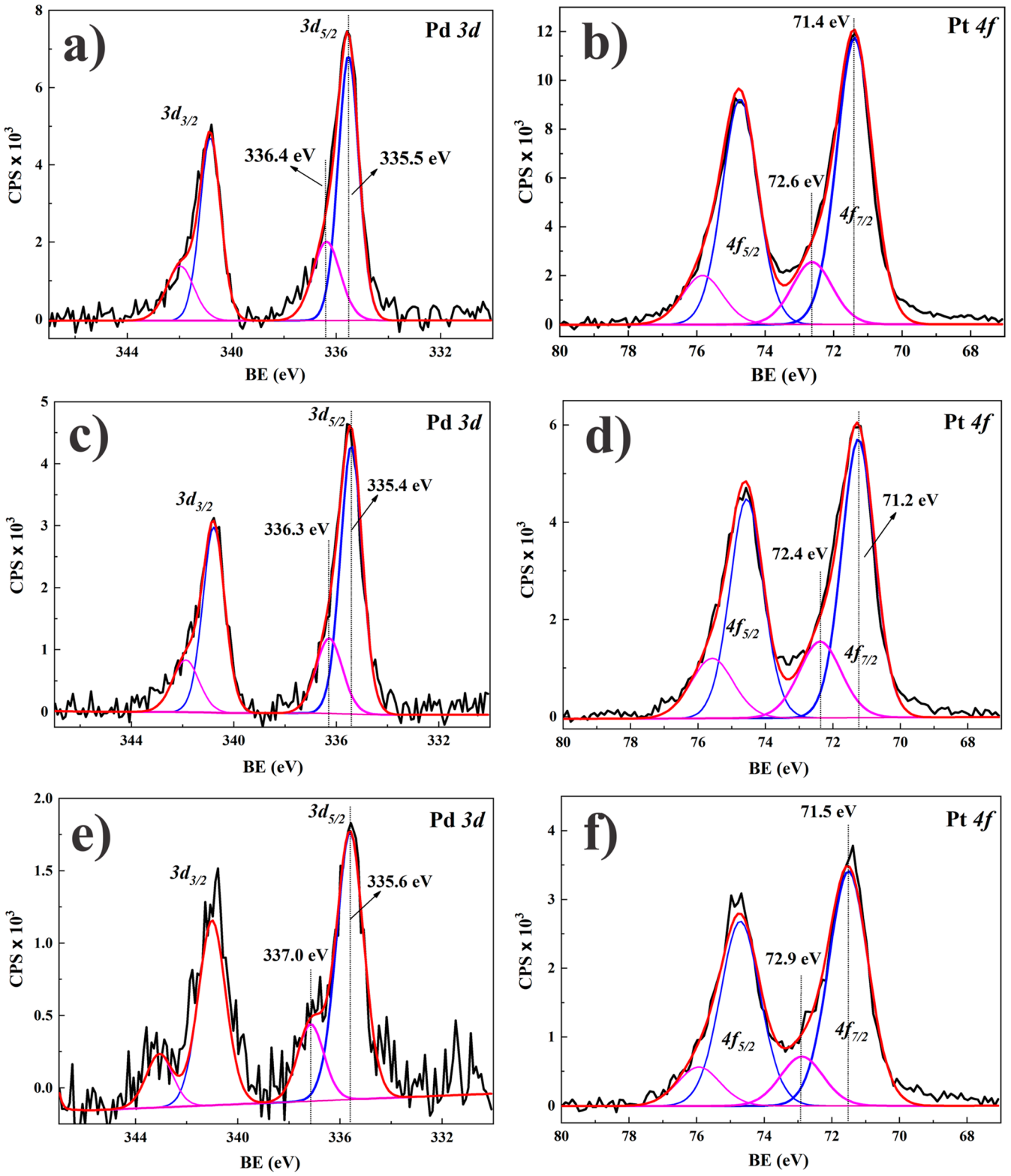

Figure 2. High-energy resolution XPS spectra showing (a) Pd 3d and (b) Pt 4f peaks of the PtPd/HPC-1 sample, (c) Pd 3d and (d) Pt 4f peaks of the PtPd/HPC-2 sample, and (e) Pd 3d and (f) Pt 4f lines of the PtPd/HPC-3 sample.

The EDX chemical analysis is presented in Figure 4. A PtPd alloy was formed, confirming the atomic concentration observed by the Rietveld refinement (Table 2), where, particles of a single element (Pt or Pd) were not found. Several particles of the HPC-2 sample were measured, and similar spectra were obtained. A representative spectrum is displayed in the inset of Figure 4. EDX maps were collected in areas of 20 × 20 nm^2 confirming alloy formation, where the elements Pt and Pd are homogeneously distributed (i.e., 50% Pt and 50% Pd). Other TEM and HRTEM measurements are presented in the Supporting Information, Figures S6−S9.

https://doi.org/10.1021/acsomega.2c01457
ACS Omega 2022, 7, 20860−20871

Table 3. BE and Percentual Atomic Concentration (at. %) Obtained from XPS Data for the Three HPC Samples

	HPC-1		HPC-2		HPC-3		
level	BE (eV)	at. %	BE (eV)	at. %	BE (eV)	at. %	binding type
C 1s	284.8	72.2	284.8	70.6	284.7	72.7	C−C/C−H_x
	286.6	11.6	286.5	11.3	286.5	11.9	C−OH
	288.9	4.3	288.9	6.1	288.9	4.2	O=C−OH
O 1s	530.7	3.5	530.7	0.9	530.3	1.3	O-metal
	532.2	5.4	532.2	4.9	532.2	7.1	OH^-
	533.3	0.6	533.7	4.1	533.7	2.0	O=C−
Pd $3d_{5/2}$	335.5	0.6	335.4	0.6	335.6	0.2	Pd−Pd (Pd^0)
	336.4	0.2	336.3	0.2	337.0	0.1	Pd−O (Pd^{2+})
Pt $4f_{7/2}$	71.4	1.4	71.2	1.0	71.5	0.5	Pt−Pt (Pt^0)
	72.6	0.3	72.4	0.3	72.9	0.1	Pt−OH (Pt^{2+})

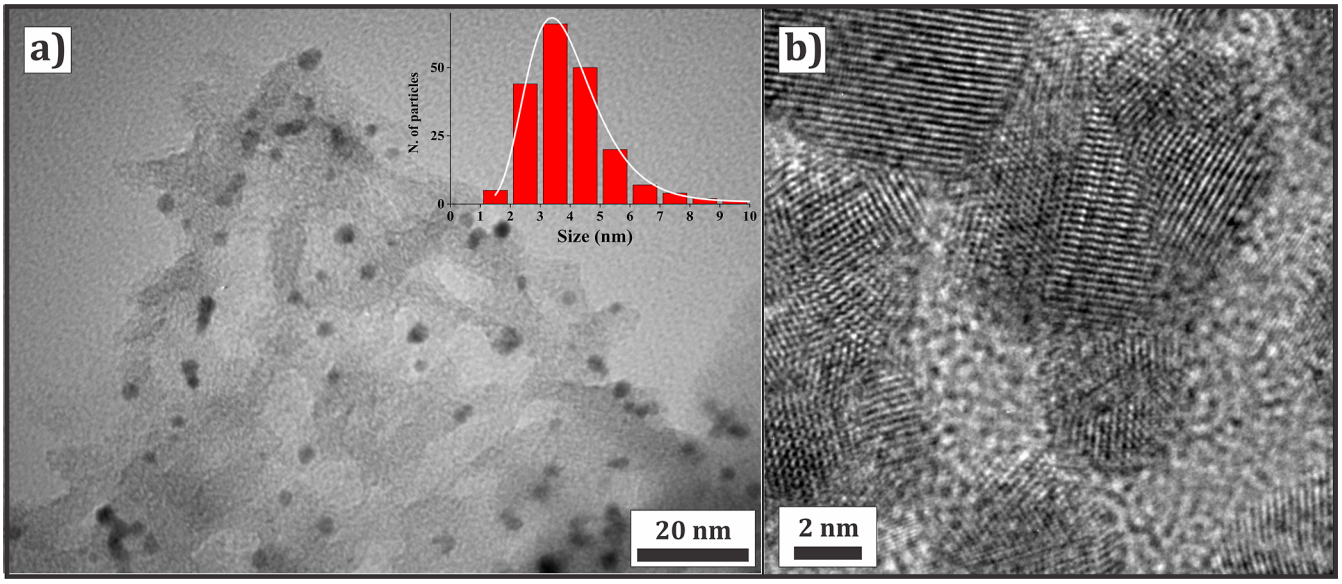

Figure 3. TEM images of (a) PtPd/HPC-2 and (b) HRTEM of PtPd-NP in HPC-2. The inset in (a) shows a representative particle diameter distribution of PtPd-NP in HPC-2 sample.

The CO stripping curves for the synthesized catalysts are presented in Figure 5a. The electrochemically active surface areas (ESA, expressed in $m^2\ g^{-1}$) are given in Table 4. PtPd/HPC-3 presents the highest surface area of 49.6 $m^2\ g^{-1}$, which suggests a better dispersion of PtPd-NP on the HPC-3 surface in contrast to PtPd/HPC-1 and PtPd/HPC-2 with ESA values of 38.8 and 40.2 $m^2\ g^{-1}$, respectively. For ORR measurements in oxygen saturated solution of H_2SO_4 0.5 mol L^{-1}, similar shapes are observed for PtPd/HPC-1 and PtPd/HPC-3, achieving a limited current at potentials more positive than PtPd/HPC-2 (Figures 5b and S10). Remarkably, materials do not follow the Koutecky−Levich approximation and both, the geometric surface area (0.0706 cm^2) and ESA values, are not appropriate for the calculation of the number of electrons involved in the process.[55,56] The hierarchical nature of the carbonaceous material (see Supporting Information) makes this calculation difficult, resulting in n values (see Table S1) that are not in good agreement with the reported values of 4 electrons for PtPd catalyst.[57−59] The main weakness is the lack of information about the real electroactive surface area (ESA) accessible for dissolved O_2 for a given condition. Even more, probably due to differences in carbon support pore size, the accessible surface (or ESA) depends on the support porosity.

Accordingly, in this work, for a suitable comparison, the polarization curves were represented by normalizing the current by PtPd mass (the active material), PtPd/HPC-2 being the catalyst with the highest value of −1285 A g^{-1} for the ORR at 1600 rpm, followed by PtPd/HPC-3 (−856 A g^{-1}) and PtPd/HPC-1 (−789 A g^{-1}) (Figure 5c).

In order to explain the use of PtPd mass for current normalization and the importance of the pore size, as well as the ESA, here, we assume that the ESA of PtPd catalysts is the main descriptor for catalysts performance. This hypothesis is reasonable and implies that current, as expressed in this text (A g^{-1}), should be finally determined by the metal surface extension for a given mass of catalysts. Given that the ESA values ($m^2\ g^{-1}$) of PtPd catalysts follow the sequence: PtPd/HPC-3 (49.6 $m^2\ g^{-1}$) > PtPd/HPC-2 (40.2 $m^2\ g^{-1}$) > PtPd/HPC-1 (38.8 $m^2\ g^{-1}$), we could expect the same trend for the mass activity, that is, PtPd/HPC-3 > PtPd/HPC-2 > PtPd/HPC-1, which is the same one we would obtain if only the pore size governed the activity. However, the results above discussed clearly show this order: PtPd/HPC-2 > PtPd/HPC-3 > PtPd/HPC-1, which, by itself, does not relieve the PtPd surface from a key role in the final result. The results interpretation, however, is not so straightforward. A tentative explanation could be given by assuming a compromise

https://doi.org/10.1021/acsomega.2c01457
ACS Omega 2022, 7, 20860−20871

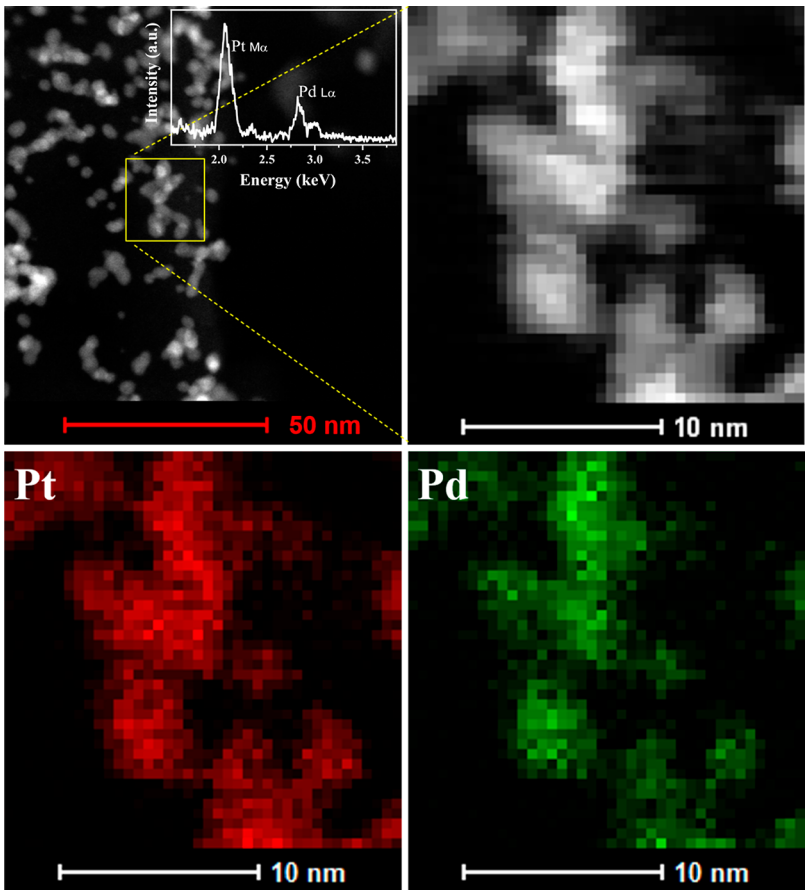

Figure 4. STEM image and zoomed region where EDX maps were collected. The inset presents a representative EDX spectrum of PtPd-NP.

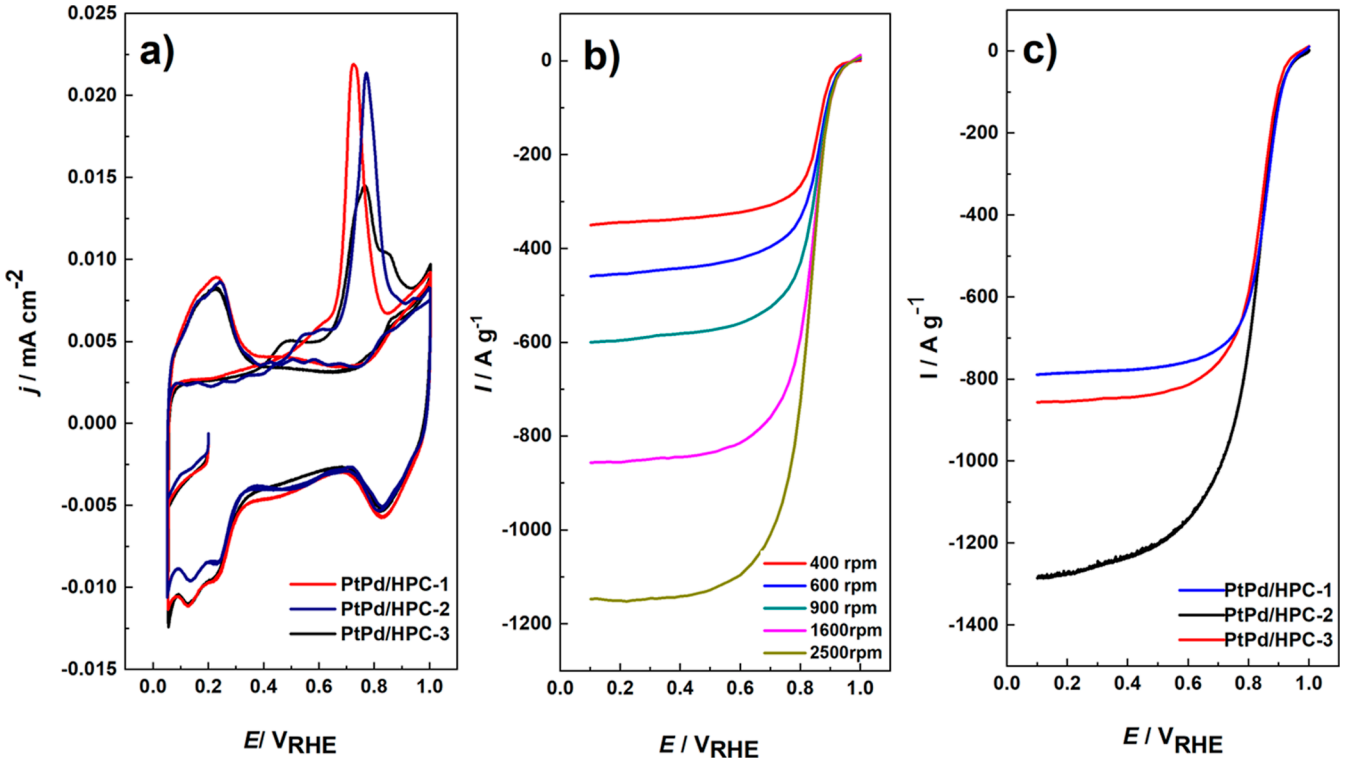

Figure 5. a) CV during CO_{ad} stripping, H_2SO_4 0.5 mol L^{-1}; E_{ad} = 0.20 V; t_{ad} = 600 s; υ = 20 mV s^{-1}. (b) LSVs in O_2-saturated H_2SO_4 0.5 mol L^{-1}, υ: 2 mV s^{-1}, at different rotary speeds (400−2500 rpm) for PtPd/HPC-3. (c) Comparison within all catalyst for ORR at ω: 1600 rpm and υ: 2 mV s^{-1}.

https://doi.org/10.1021/acsomega.2c01457
ACS Omega 2022, 7, 20860−20871

Table 4. Reported ORR Values for Different Pt or Pd Based-Catalyst Supported on Carbon Materials during the LSV Measurements at 1600 rpm

catalyst	catalyst description	ESA/m^2 g^{-1}	onset potential/V	$E_{1/2}$/V	scan velocity/mV s^{-1}	electrolyte	reference
PtPd/f-*p*-CNF	PtPd alloy catalysts supported on self-nitrogen-doped porous carbon nanofibers	69	0.95	0.826	5	0.1 mol L^{-1} $HClO_4$	33
PtPd/CKN	porous carbon-supported PtPd alloy nanoparticles derived from N-heterocyclic carbene bimetal complex		0.9	0.821	5	0.1 mol L^{-1} KOH	60
Pt/HSAG300	Pt nanoparticles supported on high surface area graphite Timcal	26.69		0.8	5	0.5 mol L^{-1} H_2SO_4	61
Pt/OMC	Pt nanoparticles supported on ordered mesoporous carbon (OMC, ACS Materials)	32.29		0.8	5	0.5 mol L^{-1} H_2SO_4	61
PdCo@NPNCs	PdCo bimetallic nanoparticles encapsulated on N-doped porous carbon nanocapsules			0.914	5	0.1 mol L^{-1} KOH	62
Pt/C	commercial Pt/C (20 wt %)	46		0.89	10	0.1 mol L^{-1} $HClO_4$	32
Pt/DPC	Pt catalyst supported on doped porous carbon nanostructure		0.9	0.83	1	0.1 mol L^{-1} $HClO_4$	63
PtPd/HPC-1	PtPd catalyst supported on HPC using SiO_2-NP of 300 nm as the template.	38.8	0.94	0.851	2	0.5 mol L^{-1} H_2SO_4	this work
PtPd/HPC-2	PtPd catalyst supported on HPC using SiO_2-NP of 400 nm as the template.	40.2	0.94	0.84	2	0.5 mol L^{-1} H_2SO_4	this work
PtPd/HPC-3	PtPd catalyst supported on HPC using SiO_2-NP of 500 nm as the template.	49.6	0.92	0.845	2	0.5 mol L^{-1} H_2SO_4	this work

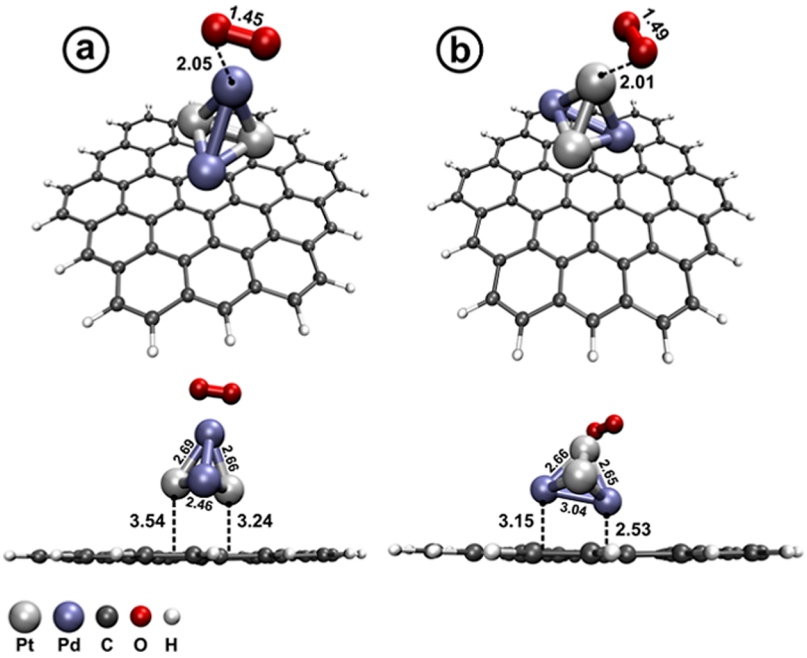

Figure 6. Optimized structures of Pt_2Pd_2 clusters interacting with a circumcoronene molecule, and oxygen through Pd (a) and Pt (b), at the M06-2X/6-311G(d)/LANL2DZ level of theory. Interatomic distances are expressed in Angstroms.

between effective diffusion lengths for dissolved oxygen in a given porous structure, and the neat PtPd catalysts load accessible in such portion of the catalytic layer. Under such a hypothesis, an improved mass transport support is also characterized by a less compact catalyst distribution. Consequently, in such an improved mass transport support (as PtPd/HPC-3) a significant portion of catalyst particles would leave out of the active layer, diminishing the performance of the catalyst as a whole. On the other hand, in the most densely packed catalysts (i.e., PtPd/HPC-1) a sufficient number of metal nanoparticles are closer to the surface, but the diffusion length provided by the porous support is now excessively short. Additional evidence supporting this hypothesis is the unusual number of electrons that results from the RDE experiments (as stated above and shown in Table S1).

In contrast with commercial Pt/C catalysts (or others supported onto the "vulcan type" carbon nanoparticles), this work explores the use of highly porous, low-density carbon as support for PtPd nanoparticles. Contrasting with the former supports, here the primary open structure of the HPC prevents further agglomeration during film formation, assuring an open, free access porous structure.

Based on the state-of-the-art Pt or Pd based-catalysts supported on carbon materials, it is observed from Table 4 that the catalysts prepared in this work are in good agreement with the previous ones reported by other authors.

https://doi.org/10.1021/acsomega.2c01457
ACS Omega 2022, 7, 20860−20871

A stability test was performed in the presence of oxygen by chronoamperometry at three different potentials: at the onset potential (at 0.9 V), after the onset (at 0.5 V), and in the diffusion-controlled region (at 0.1 V) (see Figure S11 in the Supporting Information) in H_2SO_4 0.5 mol L^{-1}. First, a decrease in the current is observed after the application of 0.9 V from an initial potential of 1.0 V, remaining positive (anodic currents) as expected and stable after 4000 s until the 7000 s of the experiment. Cathodic currents, indicating that the reduction of oxygen takes place, are recorded at 0.5 and 0.1 V. At the former potential, after a first increase, the currents remain quite stable for PtPd/HPC-1 and PtPd/HPC-2 around −2.5 and −3.7 A g^{-1}, whereas some oscillations are recorded for PtPd/HPC-3 with a continuous increase in the signal (it seems that this electrode activates with the time) achieving a final value around −6.55 A g^{-1}. Finally, at 0.1 V, the negative currents achieve more cathodic values (final currents at 7000 s are −5.2, −8.2, and −10.6 A g^{-1} for PtPd/HPC-1, PtPd/HPC-2, and PtPd/HPC-3, respectively) but the behavior with the time is different. However, PtPd/HPC-1 is quite stable, the current for PtPd/HPC-2 continuously decreases while that for PtPd/HPC-3 increases. From these curves, it seems that the catalysts are quite stable without losing stability during 2 h. Accordingly, the enhancement of the catalyst stability when the catalyst was supported on porous carbons has been previously reported.[62,64−67]

By considering a tetrahedral bimetallic cluster Pt_2Pd_2, according to the model proposed by Alexandrova et al.,[41] the interaction between the PtPd 1:1 nanoparticles with a graphitic domain of an HPC pore[68] and molecular oxygen was theoretically explored. Remarkably, this cluster corresponds to the minimum energy Pt/Pd tetramer calculated through a DFT approach and reflects the nanoparticle Pt/Pd ratio revealed by the EDX analysis for the three catalysts herein obtained (see Table 1). Two interaction situations were considered with molecular oxygen interacting through Pd (Figure 6a) or Pt (Figure 6b). The optimized structures of the three-fragments arrays are presented in Figure 6 where the cluster exhibits a distorted tetrahedral structure in both cases. The fragments calculation reveals a more stable situation when Pt_2Pd_2 interacts with oxygen through Pt (Figure 6b), with more intense Pt_2Pd_2−$C_{54}H_{18}$ (−24.8 kcal mol^{-1}) and Pt_2Pd_2−O_2 (−142.4 kcal mol^{-1}) contacts, in comparison to the Pd situation (−18.9 and −136.1 kcal mol^{-1}, respectively). The higher stability of the configuration favoring Pt−O_2 interactions is also evidenced by the shorter Pd−C interatomic distances involving the cluster and the circumcoronene molecule (2.53 and 3.15 Å), relative to the Pt−C distances in its counterpart (3.24 and 3.54 Å). On the other hand, the Pd−O (2.05 Å) and Pt−O (2.01 Å) distances are very similar and lower than the corresponding sum of van der Waals radii (Pt: 1.75 Å, Pd: 1.63 Å, and O: 1.52 Å) in line with a chemisorption process. These results suggest a more stable array when the catalyst is anchored to the HPC support through the palladium atoms, thus exposing the platinum atoms to the oxygen interaction that initiates ORR.

For the three synthetized catalysts, similar structural and surface characteristics are observed. All catalyst has a Pt/Pd ratio of 1:1 according to EDX, and from SEM and TEM measurements, the surface is composed of Pt^0/Pt^{+2} and Pd^0/Pd^{+2} (from XPS data) with a similar crystallite size of ∼5−6 nm (from XRD). Accordingly, we conclude that there are no substantial differences in PtPd-NP surface which would suggest different "inherent" catalytic activity.

Our results also indicate that there is no correlation between the neat catalyst surface and the current density obtained for all catalysts during ORR (Figure 5c and Table 4). In addition, PtPd/HPC-3 catalyst presents the highest surface/mass relationship due to the better PtPd-NP dispersion on the carbon surface (Table 4). Surprisingly, the highest surface area (m^2 g^{-1}) of PtPd/HPC-3 would demand greater mass transfer, adversely affecting the observed *j*. The experimental data, however, reveals a relationship between the current density and the primary porous structure of the support.

The single most striking observation emerging from the data comparison is that not only the porous size of carbonaceous materials is a determinant for the ORR but also the PtPd catalysts load. Therefore, the results obtained in this work reveal that a well-developed pore structure (combination of macro-mesopores) promotes the catalyst dispersion, improving its electrochemical performance in the ORR process. This effect has been observed in our previous works where HPCs have been used to support NP of PtRu, PtPd, PtFe, and PtAu for applications in FC.[45,69−72]

4. CONCLUSIONS

This work reports the synthesis of PtPd catalysts supported on HPC with different macropore sizes to be used for the study of the ORR. The CO stripping analysis shows that PtPd/HPC-3 exhibits the biggest ESA value of 49.6 m^2 g^{-1}, followed by PtPd/HPC-2 with 40.2 m^2 g^{-1} and PtPd/HPC-1 with 38.8 m^2 g^{-1}. For the three considered electrocatalysts, similar morphological and surface characteristics were observed by XRD, TEM, EDX, and XPS. The electrocatalysts were evaluated by electrochemical techniques such as cyclic voltammetry (CV) and linear scanning voltammetry for the ORR, obtaining the highest current density of −1285 A g^{-1} for the PtPd/HPC-2 catalyst in the oxygen saturated H_2SO_4 0.5 mol L^{-1} solution. The computational DFT study offers a chemically intuitive picture of the preference of oxygen for the bimetallic cluster Pt atoms, as well as the more stable configuration when the cluster interacts with the HPC through the palladium atoms. The results of this study support the idea of a synergic effect between PtPd-NP and the porous supports, where the macropores on carbon material play a key role in catalyst dispersion and performance for the ORR. Consequently, PtPd-NP supported on HPCs can be considered good candidates as cathodes in FC.

■ ASSOCIATED CONTENT

Supporting Information

The Supporting Information is available free of charge at https://pubs.acs.org/doi/10.1021/acsomega.2c01457.

Physicochemical characterization of HPC supports: DLS analysis of the template, SEM analysis of HPCs, TGA-DSC, and Raman analysis; Physicochemical characterization of PtPd/HPC-X catalysts: EDX, TEM, and TEM-EDX analysis; and Electrochemical evaluation of PtPd/HPC-X during ORR: LSV curves, electrons number obtained by Koutecky−Levich equation, and stability test (PDF)

https://doi.org/10.1021/acsomega.2c01457
ACS Omega 2022, 7, 20860−20871

AUTHOR INFORMATION

Corresponding Author

Angélica María Baena-Moncada − *Laboratorio de Investigación de Electroquímica Aplicada, Facultad de Ciencias, Universidad Nacional de Ingeniería, Rímac, Lima 15333, Perú;* orcid.org/0000-0002-2896-4392; Phone: 0051955136208; Email: abaenam@uni.edu.pe

Authors

Ofelia Marilu Arias-Pinedo − *Laboratorio de Investigación de Electroquímica Aplicada, Facultad de Ciencias, Universidad Nacional de Ingeniería, Rímac, Lima 15333, Perú*

Andy A. Cardenas Riojas − *Laboratorio de Investigación de Electroquímica Aplicada, Facultad de Ciencias, Universidad Nacional de Ingeniería, Rímac, Lima 15333, Perú*

Elena Pastor − *Departamento de Química, Instituto de Materiales y Nanotecnología, Universidad de La Laguna, La Laguna, Tenerife, Spain*

Elvis O. López − *Laboratorio de Investigación de Electroquímica Aplicada, Facultad de Ciencias, Universidad Nacional de Ingeniería, Rímac, Lima 15333, Perú; Department of Experimental Low Energy Physics, Brazilian Center for Research in Physics (CBPF), Rio de Janeiro 22290-180, Brazil*

Geronimo Perez − *Department of Engineering, Federal Fluminense University (UFF), Niteroi, Rio de Janeiro 24210-240, Brazil*

Braulio S. Archanjo − *Materials Metrology Division, National Institute of Metrology Quality and Technology (INMETRO), Rio de Janeiro 25250-020, Brazil;* orcid.org/0000-0001-8145-7712

Miguel Ponce-Vargas − *Institut de Chimie Moléculaire de Reims, Université de Reims Champagne-Ardenne, Reims 51687, France;* orcid.org/0000-0002-6028-3167

Gabriel Ángel Planes − *Facultad de Ciencias Exactas Fisicoquímicas y Naturales and Instituto de Investigaciones en Tecnologías Energéticas y Materiales Avanzados (IITEMA), Universidad Nacional de Río Cuarto, Río Cuarto, Córdoba, Argentina*

Complete contact information is available at: https://pubs.acs.org/10.1021/acsomega.2c01457

Notes

The authors declare no competing financial interest.

ACKNOWLEDGMENTS

The authors gratefully acknowledge the financial support of 2020 RESEARCH PROJECTS provided by the Research Unit of the Faculty of Sciences and the project FC-PF-02-2022 provided by the Vicerrectorado de Investigación of the Universidad Nacional de Ingeniería (National University of Engineering), Lima-Peru. The authors wish to thank the Materials Metrology Division at the Brazilian National Institute of Metrology (INMETRO) for TEM and HRTEM measurements and the Brazilian Center for Research in Physics (CBPF) for the FTIR measurements. The authors also acknowledge the MaSCA (Maison de la Simulation de Champagne-Ardenne, France) for computing facilities (http://romeo.univ-reims.fr).

REFERENCES

(1) Moriarty, P.; Honnery, D. Hydrogen's Role in an Uncertain Energy Future. *Int. J. Hydrogen Energy* **2009**, *34*, 31−39.

(2) Moriarty, P.; Honnery, D. What Is the Global Potential for Renewable Energy? *Renew. Sustain. Energy Rev.* **2012**, *16*, 244−252.

(3) Patzek, T. W.; Croft, G. D. A Global Coal Production Forecast with Multi-Hubbert Cycle Analysis. *Energy* **2010**, *35*, 3109−3122.

(4) Fawzy, S.; Osman, A. I.; Doran, J.; Rooney, D. W. Strategies for Mitigation of Climate Change: A Review. *Environ. Chem. Lett.* **2020**, *18*, 2069−2094.

(5) Abdelkareem, M. A.; Elsaid, K.; Wilberforce, T.; Kamil, M.; Sayed, E. T.; Olabi, A. Environmental Aspects of Fuel Cells: A Review. *Sci. Total Environ.* **2021**, *752*, 141803.

(6) Das, H. S.; Tan, C. W.; Yatim, A. H. M. Fuel cell hybrid electric vehicles: A review on power conditioning units and topologies. *Renew. Sustain. Energy Rev.* **2017**, *76*, 268−291.

(7) Wang, Y.; Ruiz Diaz, D. F.; Chen, K. S.; Wang, Z.; Adroher, X. C. Materials, technological status, and fundamentals of PEM fuel cells—A review. *Mater. Today* **2020**, *32*, 178−203.

(8) Acres, G. J. K. Recent Advances in Fuel Cell Technology and Its Applications. *J. Power Sources* **2001**, *100*, 60−66.

(9) Dresselhaus, M. S.; Thomas, I. L. Alternative Energy Technologies. *Nature* **2001**, *414*, 332−337.

(10) Lu, Y.; Jiang, Y.; Chen, W. PtPd Porous Nanorods with Enhanced Electrocatalytic Activity and Durability for Oxygen Reduction Reaction. *Nano Energy* **2013**, *2*, 836−844.

(11) Hou, J.; Yang, M.; Ke, C.; Wei, G.; Priest, C.; Qiao, Z.; Wu, G.; Zhang, J. Platinum-Group-Metal Catalysts for Proton Exchange Membrane Fuel Cells: From Catalyst Design to Electrode Structure Optimization. *EnergyChem* **2020**, *2*, 100023.

(12) Ren, X.; Lv, Q.; Liu, L.; Liu, B.; Wang, Y.; Liu, A.; Wu, G. Current Progress of Pt and Pt-Based Electrocatalysts Used for Fuel Cells. *Sustainable Energy Fuels* **2019**, *4*, 15−30.

(13) Zhang, C.; Shen, X.; Pan, Y.; Peng, Z. A Review of Pt-Based Electrocatalysts for Oxygen Reduction Reaction. *Front. Energy* **2017**, *11*, 268−285.

(14) Li, M.; Zhu, Y.; Song, N.; Wang, C.; Lu, X. Fabrication of Pt Nanoparticles on Nitrogen-Doped Carbon/Ni Nanofibers for Improved Hydrogen Evolution Activity. *J. Colloid Interface Sci.* **2018**, *514*, 199−207.

(15) Liu, S.; Han, L.; Zhu, J.; Xiao, W.; Wang, J.; Liu, H.; Xin, H.; Wang, D. Enhanced Electrocatalytic Activity and Stability of Pd3V/C Nanoparticles with a Trace Amount of Pt Decoration for the Oxygen Reduction Reaction. *J. Mater. Chem. A* **2015**, *3*, 20966−20972.

(16) Sun, X.; Li, D.; Ding, Y.; Zhu, W.; Guo, S.; Wang, Z. L.; Sun, S. Core/Shell Au/CuPt Nanoparticles and Their Dual Electrocatalysis for Both Reduction and Oxidation Reactions. *J. Am. Chem. Soc.* **2014**, *136*, 5745−5749.

(17) Xiong, Y.; Shan, H.; Zhou, Z.; Yan, Y.; Chen, W.; Yang, Y.; Liu, Y.; Tian, H.; Wu, J.; Zhang, H.; Yang, D. Tuning Surface Structure and Strain in Pd-Pt Core-Shell Nanocrystals for Enhanced Electrocatalytic Oxygen Reduction. *Small* **2017**, *13*, 1603423.

(18) Li, P.; Shi, E.; Yang, Y.; Shang, Y.; Peng, Q.; Wu, S.; Wei, J.; Wang, K.; Zhu, H.; Yuan, Q.; Cao, A.; Wu, D. Carbon Nanotube-Polypyrrole Core-Shell Sponge and Its Application as Highly Compressible Supercapacitor Electrode. *Nano Res.* **2014**, *7*, 209−218.

(19) Ren, Y.; Yang, X.; Li, L.; Li, C.; Zhang, X.; Lu, Z.; Yu, X. Pd@Pt Core−Shell Nanoflowers as Efficient Catalyst Toward Methanol Oxidation. *Catal. Lett.* **2020**, *150*, 3415−3423.

(20) Xu, L.; Cui, Q.; Zhang, H.; Jiao, A.; Tian, Y.; Li, S.; Li, H.; Chen, M.; Chen, F. Ultra-Clean PtPd Nanoflowers Loaded on GO Supports with Enhanced Low-Temperature Electrocatalytic Activity for Fuel Cells in Harsh Environment. *Appl. Surf. Sci.* **2020**, *511*, 145603.

(21) Cho, K. Y.; Yeom, Y. S.; Seo, H. Y.; Lee, A. S.; Huy Do, X.; Hong, J. P.; Jeong, H.-K.; Baek, K.-Y.; Yoon, H. G. Fine-Sized Pt Nanoparticles Dispersed on PdPt Bimetallic Nanocrystals with Non-Covalently Functionalized Graphene toward Synergistic Effects on the Oxygen Reduction Reaction. *Electrochim. Acta* **2017**, *257*, 412−422.

(22) Esabattina, S.; Posa, V. R.; Zhanglian, H.; Godlaveeti, S. k.; Reddy, R. R.; Somala, A. R. Fabrication of Bimetallic PtPd Alloy Nanospheres Supported on RGO Sheets for Superior Methanol Electro-Oxidation. *Int. J. Hydrogen Energy* **2018**, *43*, 4115−4124.
(23) Tan, H.; Tang, J.; Kim, J.; Kaneti, Y. V.; Kang, Y.-M.; Sugahara, Y.; Yamauchi, Y. Rational Design and Construction of Nanoporous Iron- and Nitrogen-Doped Carbon Electrocatalysts for Oxygen Reduction Reaction. *J. Mater. Chem. A* **2019**, *7*, 1380−1393.
(24) Li, Z.; Li, B.; Hu, Y.; Wang, S.; Yu, C. Highly-Dispersed and High-Metal-Density Electrocatalysts on Carbon Supports for the Oxygen Reduction Reaction: From Nanoparticles to Atomic-Level Architectures. *Mater. Adv.* **2022**, *3*, 779−809.
(25) Kone, I.; Xie, A.; Tang, Y.; Chen, Y.; Liu, J.; Chen, Y.; Sun, Y.; Yang, X.; Wan, P. Hierarchical Porous Carbon Doped with Iron/Nitrogen/Sulfur for Efficient Oxygen Reduction Reaction. *ACS Appl. Mater. Interfaces* **2017**, *9*, 20963−20973.
(26) Wu, J.; Yang, R.; Yan, W. Phosphorus-Doped Hierarchical Porous Carbon as Efficient Metal-Free Electrocatalysts for Oxygen Reduction Reaction. *Int. J. Hydrogen Energy* **2019**, *44*, 12941−12951.
(27) Yasuda, S.; Furuya, A.; Uchibori, Y.; Kim, J.; Murakoshi, K. Iron−Nitrogen-Doped Vertically Aligned Carbon Nanotube Electrocatalyst for the Oxygen Reduction Reaction. *Adv. Funct. Mater.* **2016**, *26*, 738−744.
(28) Sun, H.; Quan, H.; Pan, M.; Zhang, Z.; Zeng, Y.; Chen, D. Nitrogen-Doped Hierarchically Structured Porous Carbon as a Bifunctional Electrode Material for Oxygen Reduction and Supercapacitor. *J. Alloys Compd.* **2020**, *826*, 154208.
(29) Xue, H.; Tang, J.; Gong, H.; Guo, H.; Fan, X.; Wang, T.; He, J.; Yamauchi, Y. Fabrication of PdCo Bimetallic Nanoparticles Anchored on Three-Dimensional Ordered N-Doped Porous Carbon as an Efficient Catalyst for Oxygen Reduction Reaction. *ACS Appl. Mater. Interfaces* **2016**, *8*, 20766−20771.
(30) Pan, Q.-R.; Jiang, P.-Y.; Lai, B.-L.; Qian, Y.-B.; Huang, L.-J.; Liu, X.-X.; Li, N.; Liu, Z.-Q. Co, N Co-Doped Hierarchical Porous Carbon as Efficient Cathode Electrocatalyst and Its Impact on Microbial Community of Anode Biofilm in Microbial Fuel Cell. *Chemosphere* **2022**, *291*, 132701.
(31) Lüsi, M.; Erikson, H.; Tammeveski, K.; Treshchalov, A.; Kikas, A.; Piirsoo, H.-M.; Kisand, V.; Tamm, A.; Aruväli, J.; Solla-Gullón, J. Oxygen Reduction Reaction on Pd Nanoparticles Supported on Novel Mesoporous Carbon Materials. *Electrochim. Acta* **2021**, *394*, 139132.
(32) Venarusso, L. B.; Boone, C. V.; Bettini, J.; Maia, G. Carbon-Supported Metal Nanodendrites as Efficient, Stable Catalysts for the Oxygen Reduction Reaction. *J. Mater. Chem. A* **2018**, *6*, 1714−1726.
(33) Li, Z.; Deng, X.; Zhou, H.; Xuan, W.; Xie, Z.; Liu, F. Preparation of Self-Nitrogen-Doped Porous Carbon Nanofibers and Their Supported PtPd Alloy Catalysts for Oxygen Reduction Reaction. *J. Solid State Electrochem.* **2020**, *24*, 195−206.
(34) Harris, M. T.; Brunson, R. R.; Byers, C. H. The Base-Catalyzed Hydrolysis and Condensation Reactions of Dilute and Concentrated TEOS Solutions. *J. Non-Cryst. Solids* **1990**, *121*, 397−403.
(35) Wang, W.; Gu, B.; Liang, L.; Hamilton, W. Fabrication of Two- and Three-Dimensional Silica Nanocolloidal Particle Arrays. *J. Phys. Chem. B* **2003**, *107*, 3400−3404.
(36) Baena-Moncada, A. M.; Planes, G. A.; Moreno, M. S.; Barbero, C. A. A Novel Method to Produce a Hierarchical Porous Carbon as a Conductive Support of PtRu Particles. Effect on CO and Methanol Electrooxidation. *J. Power Sources* **2013**, *221*, 42.
(37) Darby, J. B.; Myles, K. M. A Thermodynamic Study of Solid Pd-Pt Alloys. *Metall. Mater. Trans. B* **1972**, *3*, 653−657.
(38) Frisch, M. J.; Trucks, G. W.; Schlegel, H. B.; Scuseria, G. E.; Robb, M. A.; Cheeseman, J. R.; Scalmani, G.; Barone, V.; Petersson, G. A.; Nakatsuji, H. *Gaussian 16*, Revision C. 01; Gaussian, Inc.: Wallingford CT 2016.
(39) Frisch, M.; Trucks, G. W.; Schlegel, H. B.; Scuseria, G. E.; Robb, M. A.; Cheeseman, J. R.; Scalmani, G.; Barone, V.; Mennucci, B.; Petersson, G. *Gaussian 09*, Revision a. 02; Gaussian. Inc., Wallingford, CT 2009; Vol. *200*, p 28.
(40) Zhao, Y.; Truhlar, D. G. The M06 Suite of Density Functionals for Main Group Thermochemistry, Thermochemical Kinetics, Noncovalent Interactions, Excited States, and Transition Elements: Two New Functionals and Systematic Testing of Four M06-Class Functionals and 12 Other Function. *Theor. Chem. Acc.* **2008**, *120*, 215−241.
(41) Ha, M.-A.; Dadras, J.; Alexandrova, A. Rutile-Deposited Pt−Pd Clusters: A Hypothesis Regarding the Stability at 50/50 Ratio. *ACS Catal.* **2014**, *4*, 3570−3580.
(42) Mennucci, B.; Tomasi, J.; Cammi, R.; Cheeseman, J. R.; Frisch, M. J.; Devlin, F. J.; Gabriel, S.; Stephens, P. J. Polarizable Continuum Model (PCM) Calculations of Solvent Effects on Optical Rotations of Chiral Molecules. *J. Phys. Chem. A* **2002**, *106*, 6102−6113.
(43) Mennucci, B. Polarizable Continuum Model. *Wiley Interdiscip. Rev.: Comput. Mol. Sci.* **2012**, *2*, 386−404.
(44) Tomasi, J.; Mennucci, B.; Cammi, R. Quantum Mechanical Continuum Solvation Models. *Chem. Rev.* **2005**, *105*, 2999−3094.
(45) Baena-Moncada, A.; Morales, G.; Barbero, C.; Planes, G.; Florez-Montaño, J.; Pastor, E. Formic Acid Oxidation over Hierarchical Porous Carbon Containing PtPd Catalysts. *Catalysts* **2013**, *3*, 902.
(46) Keefer, K. D. The Effect of Hydrolysis Conditions on the Structure and Growth of Silicate Polymers. *MRS Online Proceedings Library (OPL)*; Cambridge University Press, 1984; Vol. *32*.
(47) Supan, K. E.; Robert, C.; Miller, M. J.; Warrender, J. M.; Bartolucci, S. F. Thermal Degradation of MWCNT/Polypropylene Nanocomposites: A Comparison of TGA and Laser Pulse Heating. *Polym. Degrad. Stab.* **2017**, *141*, 41−44.
(48) Dresselhaus, M. S.; Jorio, A.; Hofmann, M.; Dresselhaus, G.; Saito, R. Perspectives on Carbon Nanotubes and Graphene Raman Spectroscopy. *Nano Lett.* **2010**, *10*, 751−758.
(49) Baranova, E. A.; Miles, N.; Mercier, P. H. J.; Le Page, Y.; Patarachao, B. Formic Acid Electro-Oxidation on Carbon Supported PdxPt1− x (0≥ X≥ 1) Nanoparticles Synthesized via Modified Polyol Method. *Electrochim. Acta* **2010**, *55*, 8182−8188.
(50) Ohashi, M.; Beard, K. D.; Ma, S.; Blom, D. A.; St-Pierre, J.; Van Zee, J. W.; Monnier, J. R. Electrochemical and Structural Characterization of Carbon-Supported Pt−Pd Bimetallic Electrocatalysts Prepared by Electroless Deposition. *Electrochim. Acta* **2010**, *55*, 7376−7384.
(51) Moulder, J. F.; Stickle, W. F.; Sobol, P. E.; Bomben, K. D. *Handbook of X-Ray Photoelectron Spectroscopy*; Physical Electronics Division. Perkin-Elmer Corp. Eden Prairie: MN, USA, 1992.
(52) Park, K. C.; Jang, I. Y.; Wongwiriyapan, W.; Morimoto, S.; Kim, Y. J.; Jung, Y. C.; Toya, T.; Endo, M. Carbon-Supported Pt−Ru Nanoparticles Prepared in Glyoxylate-Reduction System Promoting Precursor−Support Interaction. *J. Mater. Chem.* **2010**, *20*, 5345.
(53) Lhoest, J.-B.; Bertrand, P.; Weng, L. T.; Dewez, J.-L. Combined Time-of-Flight Secondary Ion Mass Spectrometry and X-Ray Photoelectron Spectroscopy Study of the Surface Segregation of Poly (Methyl Methacrylate)(PMMA) in Bisphenol A Polycarbonate/PMMA Blends. *Macromolecules* **1995**, *28*, 4631−4637.
(54) Tressaud, A.; Khairoun, S.; Touhara, H.; Watanabe, N. X-ray Photoelectron Spectroscopy of Palladium Fluorides. *Z. Anorg. Allg. Chem.* **1986**, *540*, 291−299.
(55) Masa, J.; Batchelor-McAuley, C.; Schuhmann, W.; Compton, R. G. Koutecky-Levich Analysis Applied to Nanoparticle Modified Rotating Disk Electrodes: Electrocatalysis or Misinterpretation. *Nano Res.* **2014**, *7*, 71−78.
(56) Wiberg, G. K. H.; Zana, A. Levich Analysis and the Apparent Potential Dependency of the Levich B Factor. *Anal. Lett.* **2016**, *49*, 2397−2404.
(57) Cai, X.; Lin, R.; Liu, X.; Zhao, Y. Effect of Heat Treatment on the Surface Structure of Pd@Pt−Ni Core-Shell Catalysts for the Oxygen Reduction Reaction. *J. Alloys Compd.* **2021**, *884*, 161059.
(58) Tzorbatzoglou, F.; Brouzgou, A.; Tsiakaras, P. Electrocatalytic Activity of Vulcan-XC-72 Supported Pd, Rh and PdxRhy toward HOR and ORR. *Appl. Catal. B Environ.* **2015**, *174*−*175*, 203−211.

https://doi.org/10.1021/acsomega.2c01457
ACS Omega 2022, 7, 20860−20871

(59) Zhu, Y.; Wang, S.; Luo, Q.; Huang, H.; Tang, S.; Du, Y. Facile Synthesis of Structurally Ordered Low-Pt-Loading Pd−Pt−Fe Nanoalloys with Enhanced Electrocatalytic Performance for Oxygen Reduction Reaction. *J. Alloys Compd.* **2021**, *855*, 157322.
(60) Li, D.; Fang, H.; Yu, J.; Xu, M.; Li, T.; Wang, J. Porous Carbon Supported PtPd Alloy Nanoparticles Derived from N-Heterocyclic Carbene Bimetal Complex as Efficient Bifunctional Electrocatalysts. *Electrochim. Acta* **2020**, *337*, 135855.
(61) Sakthivel, M.; Drillet, J.-F. An Extensive Study about Influence of the Carbon Support Morphology on Pt Activity and Stability for Oxygen Reduction Reaction. *Appl. Catal. B Environ.* **2018**, *231*, 62−72.
(62) Zhang, Z.; Liu, S.; Tian, X.; Wang, J.; Xu, P.; Xiao, F.; Wang, S. Facile Synthesis of N-Doped Porous Carbon Encapsulated Bimetallic PdCo as a Highly Active and Durable Electrocatalyst for Oxygen Reduction and Ethanol Oxidation. *J. Mater. Chem. A* **2017**, *5*, 10876−10884.
(63) Kwon, S.-H.; Lee, S.-G.; Han, S.-B.; Park, K.-W. Synergistically Enhanced Electrocatalytic Stability of Pt Catalyst Supported by Doped Porous Carbon Nanostructure for Oxygen Reduction Reaction. *Electrocatalysis* **2020**, *11*, 497−504.
(64) Carrera-Cerritos, R.; Baglio, V.; Aricò, A. S.; Ledesma-García, J.; Sgroi, M. F.; Pullini, D.; Pruna, A. J.; Mataix, D. B.; Fuentes-Ramírez, R.; Arriaga, L. G. Improved Pd Electro-Catalysis for Oxygen Reduction Reaction in Direct Methanol Fuel Cell by Reduced Graphene Oxide. *Appl. Catal. B Environ.* **2014**, *144*, 554−560.
(65) Sun, X.; He, J.; Tang, J.; Wang, T.; Guo, Y.; Xue, H.; Li, G.; Ma, Y. Structural and Electrochemical Characterization of Ordered Mesoporous Carbon-Reduced Graphene Oxide Nanocomposites. *J. Mater. Chem.* **2012**, *22*, 10900−10910.
(66) Khan, I. A.; Qian, Y.; Badshah, A.; Zhao, D.; Nadeem, M. A. Fabrication of Highly Stable and Efficient PtCu Alloy Nanoparticles on Highly Porous Carbon for Direct Methanol Fuel Cells. *ACS Appl. Mater. Interfaces* **2016**, *8*, 20793−20801.
(67) Varathan, P.; Akula, S.; Moni, P.; Sahu, A. K. Natural Aloe Vera Derived Pt Supported N-Doped Porous Carbon: A Highly Durable Cathode Catalyst of PEM Fuel Cell. *Int. J. Hydrogen Energy* **2020**, *45*, 19267−19279.
(68) Long, L.; Jiang, X.; Liu, J.; Han, D.; Xiao, M.; Wang, S.; Meng, Y. In Situ Template Synthesis of Hierarchical Porous Carbon Used for High Performance Lithium−Sulfur Batteries. *RSC Adv.* **2018**, *8*, 4503−4513.
(69) Baena-Moncada, A. M.; Coneo-Rodríguez, R.; Calderón, J. C.; Flórez-Montaño, J.; Barbero, C. A.; Planes, G. A.; Rodríguez, J. L.; Pastor, E. Macroporous Carbon as Support for PtRu Catalysts. *Int. J. Hydrogen Energy* **2014**, *39*, 3964−3969.
(70) Baena-Moncada, A. M.; Bazan-Aguilar, A.; Pastor, E.; Planes, G. Á. Methanol Conversion Efficiency to CO2</Inf> on PtRu Nanoparticles Supported Catalysts, a DEMS Study. *J. Power Sources* **2019**, *437*, 226915.
(71) Cappellari, P. S.; Baena-Moncada, A. M.; Coneo-Rodríguez, R.; Moreno, M. S.; Barbero, C. A.; Planes, G. A. Catalytic Enhancement of Formic Acid Electro-Oxidation through Surface Modifications with Gold on Supported Pt Nanoparticles. *Int. J. Hydrogen Energy* **2019**, *44*, 1967−1972.
(72) Baena-Moncada, A. M.; Coneo-Rodríguez, R.; La Rosa-Toro, A.; Pastor, E.; Barbero, C.; Planes, G. Á. PtFe Catalysts Supported on Hierarchical Porous Carbon toward Oxygen Reduction Reaction in Microbial Fuel Cells. *J. Solid State Electrochem.* **2019**, *23*, 2683.

https://doi.org/10.1021/acsomega.2c01457
ACS Omega 2022, 7, 20860−20871